IAES International Journal of Artificial Intelligence (IJ-AI)
Vol. 14, No. 1, February 2025, pp. 119~129
ISSN: 2252-8938, DOI: 10.11591/ijai.v14.i1.pp119-129

Improved adaptive multi-threshold method for automatic identification of rhinosinusitis in paranasal sinus images

Ondra Eka Putra[1], Sumijan[2], Muhammad Tajuddin[3]
[1]Department of Informatics Technology, Faculty of Computer Science, Universitas Putra Indonesia YPTK, Padang, Indonesia
[2]Doctoral Study Program Information Technology, Faculty of Computer Science, Universitas Putra Indonesia YPTK, Padang, Indonesia
[3]Department of Computer Science, Faculty of Engineering, Bumigora University, Mataram, Indonesia

Article Info

Article history:

Received Dec 12, 2023
Revised Sep 11, 2024
Accepted Sep 30, 2024

Keywords:

Automatic identification
Improved adaptive multi-threshold
Rhinosinusitis
Segmentation
Sinus paranasal

ABSTRACT

Rhinosinusitis, characterized by inflammation of the mucosa or mucous membrane within the paranasal sinuses, anatomical cavities situated in the facial bones, is the focus of this investigation. This study employs computed tomography (CT)-scan images comprising sagittal slices of the paranasal sinuses, acquired through a CT device featuring a Philips Ingenuity CT model MRC880 tube type, identified by tube serial number 163889, with a pixel value resolution of 0.24 mm. The primary objective of this research is to automatically identify and delineate rhizosinusitis-affected areas. This involves the application of multi-threshold values during the segmentation process, utilizing the improved adaptive multi-threshold (IAMT) segmentation method. The research dataset encompasses 380 slices of CT-scans derived from 10 patients displaying indications of rhinosinusitis. Analysis of the test results reveals that the smallest observed rhinosinusitis size in this study is 0.05 cm^2 on the right side, while the largest size measures 1.81 cm^2, yielding an accuracy rate of 96.66%. The magnitude of rhinosinusitis sizes serves as an indicative measure of the extent of inflammation within the paranasal sinus region, thereby suggesting a potential need for more intensive treatment interventions for the affected patients.

Corresponding Author:

Ondra Eka Putra
Department of Informatics Technology, Faculty of Computer Science, Universitas Putra Indonesia YPTK
Padang, West Sumatera, Indonesia
Email: ondraekaputra@upiyptk.ac.id

1. INTRODUCTION

Rhinosinusitis, characterized by inflammation of the mucous membrane or mucosa within the paranasal sinuses and nasal passages, represents a clinical condition with distinct manifestations [1], [2]. Predominantly, the ethmoid and maxillary sinuses are frequently affected, with a comparatively lower incidence observed in cases of sphenoid and frontal sinusitis [3], [4]. Etiologically, rhinosinusitis may arise due to allergic responses or microbial infections, inclusive of bacterial and viral agents, precipitating an impediment in the physiological flow of mucus from the sinuses to the nasal cavity [5], [6]. Rhinosinusitis has the potential to give rise to a spectrum of complications, including mucocele, pre-septal cellulitis, orbital cellulitis, subperiosteal abscess, orbital abscess, osteomyelitis, meningitis, brain abscess, subdural empyema, and venous sinus thrombosis. Untreated sinusitis may culminate in a persistent loss of olfactory function. Pathological conditions affecting the paranasal sinuses are frequently discerned through the utilization of computed tomography (CT) imaging techniques, necessitating precise and vigilant monitoring [7]. In the clinical domain, CT proves superior in the meticulous analysis and diagnosis of paranasal sinus conditions compared to traditional x-ray modalities.

The manipulation of medical images has profoundly influenced healthcare practitioners in their diagnostic endeavors and therapeutic interventions. Presently established image processing methodologies have proven markedly advantageous, assuming a pivotal role in the identification process [8]. Among the various image processing procedures, the segmentation process stands out as particularly noteworthy. Fundamentally, the quintessential facet of image processing resides in the image segmentation procedure, integral for object recognition and the application of visual image processing technology [9]. The primary objective of image segmentation is the extraction of the region of interest (ROI), achieved through either an automated or semi-automated process, with direct relevance to the objects slated for analysis [10]. The process entails the delineation of object regions within an image, distinct from the background, thereby facilitating the analysis and partitioning of the object into non-overlapping regions characterized by homogeneity in attributes such as color, texture, and intensity [11]. The outcome of the image segmentation process manifests as a binary image with dual grayscale values: black, denoted by zero (0), and white, represented by one (1). The image segmentation process introduces a discernible level of complexity in image analysis, attributable to the heterogeneous characteristics exhibited by distinct objects [12]. Various methodologies are deployed in the image segmentation process, encompassing thresholding, histogram methods, region-growing, shape-based, active contour, and statistical (clustering) approaches. Predominantly, the thresholding method finds widespread application in image segmentation procedures [13]. Thresholding serves as an image segmentation technique that leverages the grayscale variation within an image. In this segmentation process, a threshold or threshold value is requisite for the analyzed image [14]. Pixel intensity values in the image that fall below the established threshold are designated a value of 0 (black), while pixel intensity values surpassing the threshold are assigned a value of 1 (white) through the thresholding method, yielding a binary image. The application of segmentation processes via thresholding has found practical use in the medical domain for identification purposes, particularly in disease detection. Consequently, it can be expounded that the image segmentation process is instrumental in discerning organ pixels within CT-scan images.

Numerous investigations in the image processing of paranasal sinus CT-scan outcomes related to rhinosinusitis have been conducted. These studies encompass advanced techniques such as the segmentation of CT images of paranasal sinuses using the convolutional neural network (CNN) algorithm for efficient and objective measurement of sinus opacification [15]. However, the proposed method faces limitations in determining the volume segmentation of individual paranasal sinus areas. Another notable approach is the automatic segmentation method of the maxillary sinus based on the visual geometry group (VGG) network, achieving a high segmentation efficiency of 94.40%. Yet, this research primarily focuses on discerning the presence or absence of maxillary sinuses in CT images. In the realm of 3D reconstruction and automatic segmentation, the use of the level set method (LSM) as a segmentation technique has been applied to the maxillary sinus and inferior concha from CT images. The segmentation coefficients obtained are impressive, with 96.3% for the inferior turbinate and 95.1% for the maxillary sinus [16]. However, this study exclusively calculates the volume of the maxillary sinus and inferior turbinate, omitting the assessment of mucous volume in the impacted area. Moreover, diagnosis through multi-view radiographs is limited to determining the presence of sinusitis in each sinus area, lacking the capability to quantify the extent of the rhinosinusitis-affected area [17]. Recent advancements include the application of semi-supervised deep learning semantic segmentation for paranasal sinus CT images in the axial view. This involves dividing the convolutional layer into two subtasks: the depthwise convolution layer, which filters input, and the pointwise convolution layer with a 1×1 filter that amalgamates filtered values to generate new features [18]. This study advocates for the development of adaptive threshold segmentation for segmenting and automatically identifying rhinosinusitis in sagittal view CT-scan images of paranasal sinuses. The findings demonstrate that this method can accurately identify and determine the surface area of rhizosinusitis, rendering it a recommended model for medical professionals to evaluate the severity of rhizosinusitis in subsequent treatment management.

2. METHOD

The data for this study comprises secondary data obtained from sagittal-view CT-scan results of paranasal sinuses in patients suffering from rhinosinusitis. Clinically, CT provides a more accurate analysis and diagnosis of paranasal sinuses than conventional x-rays. CT is considered a modality for depicting the anatomy of paranasal sinuses and proves highly useful in subsequent planning and follow-up actions [19]. Patients underwent scanning using a CT-scan device in the Department of Radiology at RSUP M. Djamil Padang, Padang City, West Sumatra, Indonesia. The tested dataset includes 380 images from 10 different patients. The processed CT-scan images are sagittal slice images in JPEG format, acquired using a CT device with a tube model CT-scan Philips Ingenuity CT, type MRC880, and tube serial number 163889. The configuration of the CT-scan results from the Philips Ingenuity CT for sagittal-view paranasal sinuses can be observed in Figure 1. Figure 1(a) represents an image of the maxillary sinus area, while Figure 1(b) displays

the maxillary sinus with rhinosinusitis. Subsequently, an adaptive multi-thresholding development model was applied for the automatic identification of rhinosinusitis in the paranasal sinuses, as depicted in Figure 2.

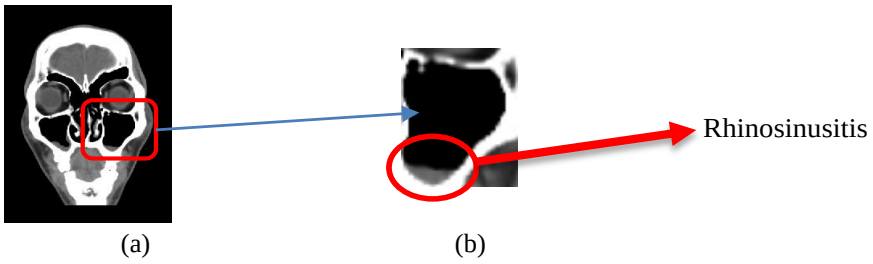

Figure 1. Paranasal sinus CT-scan sagittal view (a) paranasal sinus CT-scan of patients with rhinosinusitis and (b) rhinosinusitis

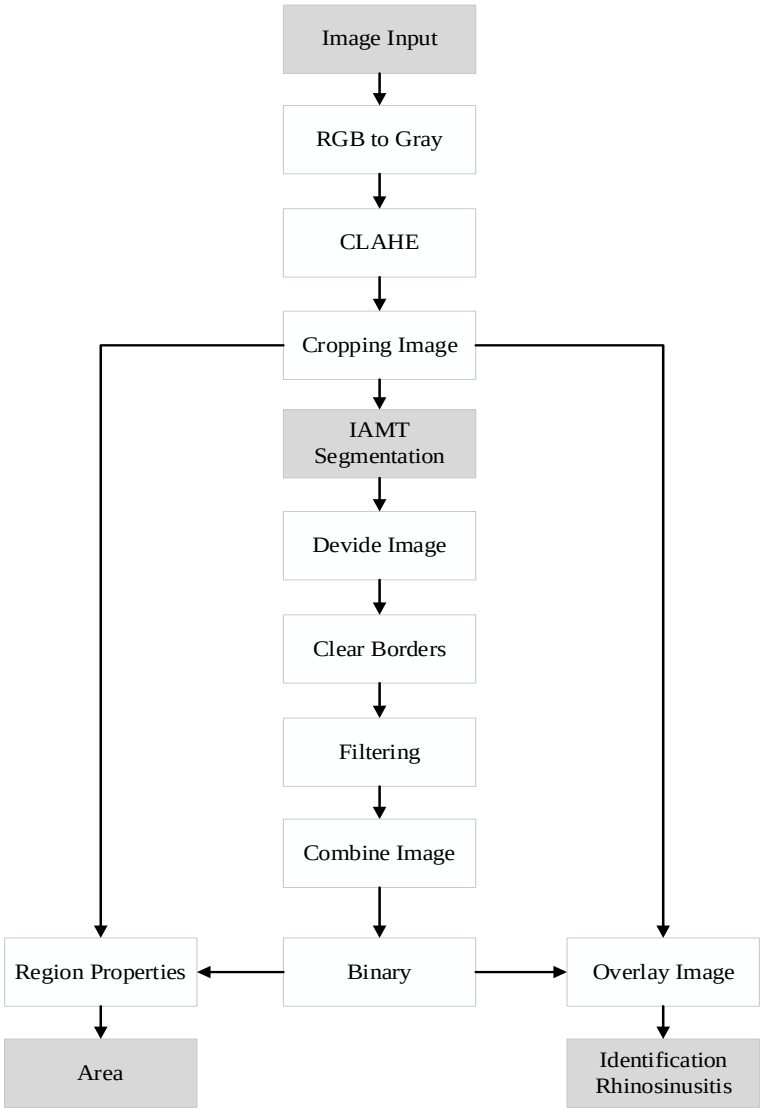

Figure 2. Research framework

Figure 2 illustrates the framework of the automatic research model for identifying rhinosinusitis through the processing of images from sagittal-view CT-scan results of paranasal sinuses. This model is

developed with multiple stages of image processing aimed at producing accurate and precise outputs. The processing stages encompass the conversion of red, green, and blue (RGB) images to grayscale, image cropping, image enhancement, segmentation operations, and extraction.

2.1. Image enhancement

Contrast limited adaptive histogram equalization (CLAHE) is a method for enhancing image quality, particularly in medical images, designed to ameliorate low contrast in the images. Adaptive histogram equalization (AHE) can introduce noise artifacts in smooth regions of the image due to excessively enhancing contrast in those areas [20]. The method employed to eliminate noise artifacts is CLAHE. The CLAHE method calculates the intensity histogram of the image by dividing the input image into non-overlapping sub-blocks [21]. A clip limit in the CLAHE method is set to cut off specific values in the histogram, smoothing the image by eliminating noise in the histogram and resulting in high-contrast levels [22]. The clip limit value is determined using a formula derived from the Rayleigh distribution process, presented in (1) [23].

$$cl = cl_{\min} + \left[2(\alpha^2) in \left(\frac{1}{1-DP(f)}\right)\right] \quad (1)$$

In this detailed analysis, clmin is defined as the minimum value that a pixel can attain within the image processing framework, serving as a critical threshold for the contrast enhancement procedure. The term DP(f) signifies a non-negative real scalar, which plays a pivotal role in calculating the distribution parameter, essential for adjusting the image's contrast based on localized regions. Furthermore, cl refers to the clip limit value, a predefined threshold that prevents over-amplification of contrast in the AHE process, ensuring that the enhancement remains within visually acceptable bounds. This process, known as CLAHE, is graphically illustrated in Figure 3 [24].

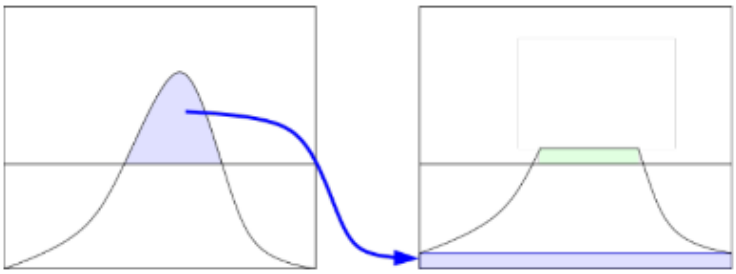

Figure 3. The illustration process of CLAHE

2.2. Cropping images

Cropping images can be employed to display the most crucial regions of an image, resulting in an improved composition for enhanced object visibility [25]. Image cropping can be executed using various methods, both manual and automatic, in the field of image processing [26]. The determination of the detected object area from the image is achieved using a binary thresholding algorithm. Binary thresholding is an image processing technique used to convert grayscale images into binary images [27]. This technique relies on the utilization of a threshold value to segregate image pixels into two categories: in the first category, pixels are assigned a value of 0 (black) if the pixel intensity is less than or equal to the threshold value, while in the second category, pixels are assigned a value of 1 (white) if the pixel intensity is greater than the threshold value [28]. The formula used to convert grayscale images into binary images using the thresholding algorithm is depicted in (2) [29].

$$ag(x,y) = \begin{Bmatrix} 0, if\ np(x,y) < NA \\ 1, if\ np(x,y) \geq NA \end{Bmatrix} \quad (2)$$

In this analytical framework, np(x,y) is identified as the input pixel value, which is the original intensity value of a pixel located at coordinates (x,y) in a grayscale image. The term ag(x,y) represents the pixel value obtained subsequent to the application of the thresholding process, effectively transforming the grayscale pixel into a binary state based on a specified threshold. NA signifies the threshold value, a critical parameter that determines the cutoff point at which pixel values are classified as either black or white, thereby

converting the entire grayscale image into a binary format. This binary conversion process, facilitated by the thresholding algorithm, is vividly illustrated in Figure 4, showcasing the transformation from nuanced grayscale images to stark binary contrasts, which is particularly useful in various image processing and computer vision tasks for simplifying analysis and enhancing feature detection.

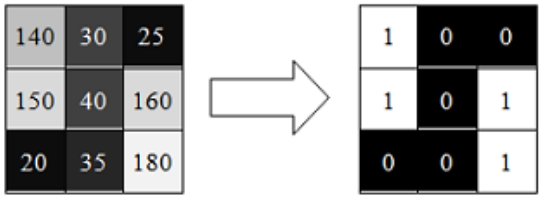

Figure 4. The illustration process of binary image

After the application of binary thresholding to segment objects within an image, the process of object detection identifies specific items of interest by delineating their coordinate boundaries. This precise identification allows for the automatic cropping of the image to focus exclusively on the detected object, a procedure that meticulously extracts the ROI without altering the inherent pixel values of the object itself. This preservation of pixel integrity is crucial, particularly in fields such as medical imaging, where the accurate representation of details can be vital for disease diagnosis and analysis. By maintaining the original pixel values within the cropped area, the image remains a reliable source for further diagnostic procedures or analytical processes, ensuring that the quality and informational content necessary for identifying and assessing medical conditions are not compromised.

2.3. Improved adaptive multi threshold segmentation

Segmentation is utilized for pixel-level classification in an image to assign appropriate categories to each pixel [30]. Image segmentation is performed to decompose an image into segments, grouping images in the process based on pixel characteristics. Image segmentation entails separating the background and foreground of an image based on shape or color similarities [31]. The image segmentation process is conducted to alleviate image complexity. In this study, the segmentation process employs an enhanced adaptive thresholding method known as improved adaptive multi-threshold (IAMT). Standard deviation intensity serves as a statistical measure describing the extent to which pixel intensities in the image are distributed or vary from the average pixel intensity value. Standard deviation indicates the level of variation or dispersion in pixel intensity data. The formula for calculating mean intensity is presented in (3), and the formula for calculating standard deviation intensity is expressed in (4).

$$\mu = \frac{\sum_{i=0}^{255} h[i]}{n} \tag{3}$$

$$\sigma = \sqrt{\frac{\sum_{i=0}^{255} (i-\mu)^2 * h[i]}{n}} \tag{4}$$

Where μ represents mean intensity, h[i] denotes the image histogram, n signifies the total number of pixels, and σ corresponds to standard deviation intensity. Standard deviation intensity elucidates how extensively pixels in the image are dispersed around the mean value. A larger standard deviation value implies a greater variation in pixel intensities in the image. Conversely, a smaller standard deviation indicates that pixel intensities tend to exhibit less variation or consistency. Employing standard deviation assists in accommodating the existing intensity variations in the image, facilitating the adjustment of the threshold to the characteristic pixel intensity of the image. After computing the mean intensity and standard deviation intensity, the subsequent step involves determining the value of the intensity control factor interval. In this study, the value of the intensity control factor interval is automatically computed as half of the standard deviation intensity value. The formula for calculating the value of the intensity control factor interval is presented in (5).

$$k = \frac{\sigma}{2} \tag{5}$$

Where k is the intensity control factor interval. Calculating the intensity control factor interval value as half of the standard deviation ensures an even distribution of intensity ranges among the threshold limits, aligning

with the desired number of threshold limits. An interval that is too large or too small can lead to suboptimal segmentation or the loss of crucial information in the image. σ represents standard deviation intensity. The results of calculating mean intensity and the intensity control factor interval are utilized to determine the optimal multi-threshold values in developing the IAMT segmentation. In multi-threshold development, more than two threshold values are employed to divide the pixel intensity range into several segments or levels. The formulas for IAMT are presented in (6) to (8).

$$T1 = \mu(x) - \left(\frac{1}{2}\right) * k \tag{6}$$

$$T2 = \mu(x) + \left(\frac{1}{2}\right) * k \tag{7}$$

$$g(x) = \begin{cases} 0, & f(i,j) < T1 \\ 1, & T1 \leq f(i,j) < T2 \\ 0, & f(i,j) \geq T2 \end{cases} \tag{8}$$

T1 is the first threshold value, T2 is the second threshold value, μ is the mean intensity used as a reference or midpoint to distinguish pixels considered as objects and background in the image. Pixels with intensities below the mean intensity are labeled as background, while pixels with intensities above the mean intensity are considered as objects. k is the interval value used to divide the pixel intensity range into segments that correspond to the specified number of threshold limits. The intensity control factor interval is the distance between each threshold limit used to separate intensity levels. $f(i,j)$ is the input grayscale image, $g(x)$ is the binary output image. If the pixel value T1 is greater than the input grayscale image or if the pixel value T2 is less than or equal to the input grayscale image, the pixel value will be changed to 0. The pixel value will be changed to 1 if the pixel value of the grayscale is greater than or equal to T1 and the pixel value of the grayscale is less than T2.

2.4. Extraction

The goal of image extraction is to reduce the dimensions of image data and extract essential features that can be used in identification [32]. The initial step in image extraction in this study is to divide the image. Divide image is a method to split the image into several parts or separate specific portions of the image. Divide image is performed to separate the image into 4 equal parts based on the multi-threshold results, where part 1 is the bottom right part of the image, part 2 is the bottom left part of the image, part 3 is the top right part of the image, and part 4 is the top left part of the image. After dividing the image, the next step involves cleaning the border area using morphological operations on parts 3 and 4, while parts 1 and 2 are assigned a value of 0 (black) as they are not the target area. After cleaning the border area, objects that are not the target are removed from parts 3 and 4 using filtering methods. The object identification process is the final stage of this research model, involving the labeling of each object and utilizing the region properties function (regionprops). Regionprops is employed to measure a set of properties for each labeled region in the label matrix. Regionprops can only detect objects with a white color as the foreground, having pixels with a value of 1, while the background is represented by pixels with a value of 0 for the black color. Major axis length represents the farthest distance from the centroid to the outermost pixel, while the minor axis length represents the closest distance from the centroid to the outermost pixel, thus obtaining the value. The representation of regions using the elliptical shape approach is presented in Figure 5.

Figure 5. Region that representation using an elliptical shape approach

3. RESULTS AND DISCUSSION

The test data for this research comprises 38 sagittal-view CT-scan images of the paranasal sinuses from a single patient with rhinosinusitis. Out of these 38 images, 7 slices were selected, indicating rhinosinusitis, specifically slices 15 to 21, based on the CT-scan. The input images are in JPG format, sized 666×512, converted from DICOM-format images obtained from the CT-scan. The shape of the input image is presented in Figure 6. Figure 6 depicts the RGB image resulting from the sagittal-view CT-scan of the paranasal sinuses, serving as input images for rhinosinusitis identification. The RGB input image is converted into a grayscale image, followed by the image quality enhancement process using the CLAHE method, aiming to eliminate noise artifacts and enhance image intensity. The enhanced image process is displayed in Figure 7, where Figure 7(a) represents the grayscale image, and Figure 7(b) represents the image after the enhancement process.

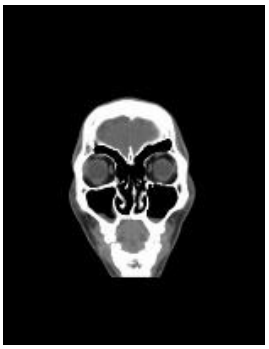

Figure 6. Input image

(a)

(b)

Figure 7. Enhancement process (a) grayscale image result and (b) CLAHE result

Figure 7 represents the image resulting from the enhancement process using the CLAHE method, aimed at achieving better image quality. Changes in image quality can be observed in the altered pixel values, and the pixel value changes for image quality enhancement are presented in Table 1. Table 1 illustrates the changes in pixel intensity values between the grayscale image and the image enhanced using the CLAHE method. Following the enhancement process, cropping is performed to obtain an image with a better composition for a closer view of the object. The subsequent step involves reducing the image complexity to separate the background from the foreground using the IAMT segmentation method to automatically obtain multi-threshold values using (6) and (7). This process results in a binary image. If the pixel value T1 is greater than the input grayscale image or if the pixel value T2 is less than or equal to the input grayscale image, the pixel value will be changed to 0. The pixel value will be changed to 1 if the grayscale pixel value is greater than T1 and less than T2. The results of the IAMT segmentation process are presented in Table 2. The research results that we obtained during this research are better compared to the results of previous research that were compared from the mean-square error (MSE) [18] and peak signal-to-noise ratio (PSNR) [22] values. Table 2 shows a comparison of the results of the MSE and PNSR test values of the current research with previous research.

Table 1. Intensity value

Grayscale image						Image enhancement with CLAHE					
1	42	89	124	153	200	7	43	88	132	159	200
18	70	106	138	175	234	23	67	110	146	179	228
42	88	121	154	208	255	42	86	129	160	206	255
72	103	135	174	238	255	68	106	143	178	231	255
91	118	154	206	253	255	90	126	161	205	248	255
107	135	173	240	255	255	111	144	177	233	255	255
119	149	201	255	255	255	127	157	201	255	255	255
131	169	232	255	253	255	141	174	227	255	248	255
146	189	255	255	255	255	154	192	255	255	255	255
153	218	255	255	255	255	161	215	255	255	255	255
169	248	255	255	255	255	175	240	255	255	255	255
187	254	255	255	255	255	191	251	255	255	255	255

Table 2. The result of segmentation image using IAMT

Slice	Image of Cropping Results	Adaptive Threshold			Improved Adaptive Multi Threshold			
		Image Result	MSE Value	PSNR Value	Image Result	MSE Value	PSNR Value	T1/T2
Slice 15			57871.35	0.50617		13844.696	6.718	6.718
Slice 16			57683.43	0.52029		15065.490	6.351	6.351
Slice 17			57372.48	0.544		15518.50	6.22	6.22
Slice 18			57272.13	0.55137		15880.40	6.12	6.12
Slice 19			57222.97	0.56		16996.93	5.83	5.83
Slice 20			57058.09	0.57		18516.8	5.46	5.46
Slice 21			57022.39	0.57		19644.23	5.2	5.2

Table 2 illustrates the outcomes of the IAMT segmentation method development process, yielding a binary image. Each input image automatically acquires distinct multi-threshold values, precisely with 2 threshold values. Subsequently, an object extraction process is conducted to automatically eliminate unnecessary objects in rhinosinusitis identification. The subsequent step involves calculating the rhinosinusitis

area from the extracted image by counting the intensity of pixels with a value of 1 (white), where each pixel corresponds to 0.24 mm. Pixels identified as rhinosinusitis have their values changed to red. The results of rhinosinusitis identification, extraction, and area calculation are displayed in Table 3.

Table 3 presents the outcomes of rhinosinusitis identification and area calculation, achieved with an exceptionally high accuracy of 96.66%. The accuracy level is computed by dividing the number of images identified with rhinosinusitis by the total number of test images and multiplying the result by 100%. The accuracy calculation for rhinosinusitis identification employs the formula displayed in (9).

$$Accuracy\ \% = \frac{\sum Rhinosinusitis}{\sum Data\ Testing} x100\% \quad (9)$$

The smallest rhinosinusitis size in this study is 0.05 cm2 on the right side, while the largest size is 1.81 cm^2. A greater rhinosinusitis size indicates a more severe identification of rhinosinusitis. The segmentation method proposed in this study can automatically identify rhinosinusitis objects and provide precise and accurate information on the rhinosinusitis area. This research introduces innovation in the image segmentation process in paranasal sinus CT-scans, making a significant contribution as an alternative solution in rhinosinusitis diagnosis. Additionally, the study ensures precision in decision-making for the treatment process of rhinosinusitis patients.

Table 3. The result of identification, extraction, and rhinosinusitis area

Slice	Result of rhinosinusitis extraction	Rhinosinusitis identification	Pixel area		Rhinosinusitis area (cm^2)	
			Left	Right	Left	Right
Slice 15			297	20	0.71	0.05
Slice 16			315	157	0.76	0.38
Slice 17			249	322	0.60	0.77
Slice 18			215	419	0.52	1.01
Slice 19			281	390	0.67	0.94
Slice 20			651	292	1.56	0.70
Slice 21			753	230	1.81	0.55

4. CONCLUSION

The development of the IAMT segmentation method for detecting rhinosinusitis provides precise and accurate identification with an accuracy rate of 96.66%. The advancement of segmentation methods in this research can maximize the performance of rhinosinusitis identification processes and deliver information about the rhinosinusitis area. The results of the proposed segmentation method development also contribute new insights into automatically calculating multi-threshold values in each patient's test image. Overall, this research makes a significant contribution to the medical field in making informed decisions for the subsequent treatment of rhinosinusitis.

ACKNOWLEDGEMENTS

We would like to express my gratitude to Dr. Zerni Melmusi, MM, Ak, CA, the Chairwoman of the Computer Higher Education Foundation in Padang, for providing substantial material support for this research. Special thanks to Dr. Tuti Handayani, Sp. Rad., a Radiologist at RSUP DR. M. Djamil Padang, West Sumatra, for validating the results of this research as an expert. The research was conducted with the approval of the Faculty of Computer Science at UPI-YPTK Padang (0248/UPI-YPTK/WRI.KL/XI/2022) and a letter from the Head of the Research and Development Unit at RSUP DR. M. Djamil Padang (No. LB.02.02/5.7/197/2023).

REFERENCES

[1] J. Xu, S. Wang, Z. Zhou, J. Liu, X. Jiang, and X. Chen, "Automatic ct image segmentation of maxillary sinus based on vgg network and improved v-net," *International Journal of Computer Assisted Radiology and Surgery*, vol. 15, no. 9, pp. 1457–1465, Sep. 2020, doi: 10.1007/s11548-020-02228-6.

[2] W. J. Fokkens *et al.*, *European position paper on rhinosinusitis and nasal polyps 2020*, Rhinology Journal, vol. 58. Amsterdam, Netherlands, 2020. doi: 10.4193/Rhin20.600.

[3] S. F. H. Naqvi, N. Arshad, M. A. Naeem, N. Waseem, N. Batool, and A. Ali, "Paranasal sinuses in the evaluation of sinusitis using computed tomography: cross sectional study," *Scholars Journal of Applied Medical Sciences*, vol. 9, no. 4, pp. 605–611, Apr. 2021, doi: 10.36347/sjams.2021.v09i04.024.

[4] Z. Saghir, A. John, A. Ali, A. Ansar, N. S. Nadeem, and H. M. Cheema, "Pathologies of paranasal sinuses diagnosed on computed tomography," *Pakistan BioMedical Journal*, vol. 5, no. 12, pp. 17–20, Dec. 2022, doi: 10.54393/pbmj.v5i12.836.

[5] T. Çatlı, H. Atilla, and E. K. Miller, "Acute viral rhinitis," in *All Around the Nose*, Cham: Springer International Publishing, 2020, pp. 199–202. doi: 10.1007/978-3-030-21217-9_23.

[6] I. Wirasati, Z. Rustam, and V. V. P. Wibowo, "Combining convolutional neural network and long short-term memory to classify sinusitis," in *2020 International Conference on Decision Aid Sciences and Application (DASA)*, IEEE, Nov. 2020, pp. 991–995. doi: 10.1109/DASA51403.2020.9317280.

[7] D. Erdem, M. Arıcıgil, and D. Chua, "Complications of rhinosinusitis," in *All Around the Nose*, Cham: Springer International Publishing, 2020, pp. 221–228. doi: 10.1007/978-3-030-21217-9_26.

[8] J. Wang, H. Zhu, S.-H. Wang, and Y.-D. Zhang, "A review of deep learning on medical image analysis," *Mobile Networks and Applications*, vol. 26, no. 1, pp. 351–380, Feb. 2021, doi: 10.1007/s11036-020-01672-7.

[9] L. Qingge, R. Zheng, X. Zhao, W. Song, and P. Yang, "An improved otsu threshold segmentation algorithm," *International Journal of Computational Science and Engineering*, vol. 22, no. 1, 2020, doi: 10.1504/IJCSE.2020.10029225.

[10] K. K. D. Ramesh, G. K. Kumar, K. Swapna, D. Datta, and S. S. Rajest, "A review of medical image segmentation algorithms," *EAI Endorsed Transactions on Pervasive Health and Technology*, vol. 7, no. 27, Apr. 2021, doi: 10.4108/eai.12-4-2021.169184.

[11] X. Liu, L. Song, S. Liu, and Y. Zhang, "A review of deep-learning-based medical image segmentation methods," *Sustainability*, vol. 13, no. 3, Jan. 2021, doi: 10.3390/su13031224.

[12] B. Lei and J. Fan, "Image thresholding segmentation method based on minimum square rough entropy," *Applied Soft Computing*, vol. 84, Nov. 2019, doi: 10.1016/j.asoc.2019.105687.

[13] S. Minaee, Y. Y. Boykov, F. Porikli, A. J. Plaza, N. Kehtarnavaz, and D. Terzopoulos, "Image segmentation using deep learning: a survey," *IEEE Transactions on Pattern Analysis and Machine Intelligence*, vol. 44, no. 7, 2021, doi: 10.1109/TPAMI.2021.3059968.

[14] B. Khorram and M. Yazdi, "A new optimized thresholding method using ant colony algorithm for mr brain image segmentation," *Journal of Digital Imaging*, vol. 32, no. 1, pp. 162–174, Feb. 2019, doi: 10.1007/s10278-018-0111-x.

[15] S. M. Humphries *et al.*, "Volumetric assessment of paranasal sinus opacification on computed tomography can be automated using a convolutional neural network," *International Forum of Allergy & Rhinology*, vol. 10, no. 11, pp. 1218–1225, Nov. 2020, doi: 10.1002/alr.22588.

[16] C.-F. J. Kuo, Y.-S. Leu, D.-J. Hu, C.-C. Huang, J.-J. Siao, and K. B. P. Leon, "Application of intelligent automatic segmentation and 3d reconstruction of inferior turbinate and maxillary sinus from computed tomography and analyze the relationship between volume and nasal lesion," *Biomedical Signal Processing and Control*, vol. 57, Mar. 2020, doi: 10.1016/j.bspc.2019.101660.

[17] Y. Jeon *et al.*, "Deep learning for diagnosis of paranasal sinusitis using multi-view radiographs," *Diagnostics*, vol. 11, no. 2, Feb. 2021, doi: 10.3390/diagnostics11020250.

[18] C.-F. J. Kuo, Y.-S. Liao, J. Barman, and S.-C. Liu, "Semi-supervised deep learning semantic segmentation for 3d volumetric computed tomographic scoring of chronic rhinosinusitis: clinical correlations and comparison with lund-mackay scoring," *Tomography*, vol. 8, no. 2, pp. 718–729, Mar. 2022, doi: 10.3390/tomography8020059.

[19] A. Nautiyal, A. Narayanan, D. Mitra, T. Honnegowda, and Sivakumar, "Computed tomographic study of remarkable anatomic variations in paranasal sinus region and their clinical importance - a retrospective study," *Annals of Maxillofacial Surgery*, vol. 10, no. 2, 2020, doi: 10.4103/ams.ams_192_19.

[20] P. Singh, R. Mukundan, and R. D. Ryke, "Feature enhancement in medical ultrasound videos using contrast-limited adaptive histogram equalization," *Journal of Digital Imaging*, vol. 33, no. 1, pp. 273–285, Feb. 2020, doi: 10.1007/s10278-019-00211-5.

[21] G. Ulutas and B. Ustubioglu, "Underwater image enhancement using contrast limited adaptive histogram equalization and layered difference representation," *Multimedia Tools and Applications*, vol. 80, no. 10, pp. 15067–15091, Apr. 2021, doi: 10.1007/s11042-020-10426-2.
[22] Sonali, S. Sahu, A. K. Singh, S. P. Ghrera, and M. Elhoseny, "An approach for de-noising and contrast enhancement of retinal fundus image using clahe," *Optics & Laser Technology*, vol. 110, pp. 87–98, Feb. 2019, doi: 10.1016/j.optlastec.2018.06.061.
[23] U. K. Acharya and S. Kumar, "Genetic algorithm based adaptive histogram equalization (gaahe) technique for medical image enhancement," *Optik*, vol. 230, Mar. 2021, doi: 10.1016/j.ijleo.2021.166273.
[24] J. Na'am, F. S. Pranata, R. Hidayat, A. M. Adif, and Ellyzarti, "Automated identification model of ground-glass opacity in ct-scan image by covid-19," *International Journal on Advanced Science, Engineering and Information Technology*, vol. 11, no. 2, pp. 595–602, Apr. 2021, doi: 10.18517/ijaseit.11.2.14143.
[25] A. Fajar, R. Sarno, C. Fatichah, and A. Fahmi, "Reconstructing and resizing 3d images from dicom files," *Journal of King Saud University - Computer and Information Sciences*, vol. 34, no. 6, pp. 3517–3526, Jun. 2022, doi: 10.1016/j.jksuci.2020.12.004.
[26] H. Carrión, M. Jafari, M. D. Bagood, H. Yang, R. R. Isseroff, and M. Gomez, "Automatic wound detection and size estimation using deep learning algorithms," *PLOS Computational Biology*, vol. 18, no. 3, Mar. 2022, doi: 10.1371/journal.pcbi.1009852.
[27] S. Iqbal, W. Khan, A. Alothaim, A. Qamar, A. Alhudhaif, and S. Alsubai, "Proving reliability of image processing techniques in digital forensics applications," *Security and Communication Networks*, vol. 2022, pp. 1–17, Mar. 2022, doi: 10.1155/2022/1322264.
[28] R. Rout and P. Parida, "Transition region based approach for skin lesion segmentation," *Procedia Computer Science*, vol. 171, pp. 379–388, 2020, doi: 10.1016/j.procs.2020.04.039.
[29] G. K. Chadha, A. Srivastava, A. Singh, R. Gupta, and D. Singla, "An automated method for counting red blood cells using image processing," *Procedia Computer Science*, vol. 167, pp. 769–778, 2020, doi: 10.1016/j.procs.2020.03.408.
[30] R. Wang, T. Lei, R. Cui, B. Zhang, H. Meng, and A. K. Nandi, "Medical image segmentation using deep learning: a survey," *IET Image Processing*, vol. 16, no. 5, pp. 1243–1267, Apr. 2022, doi: 10.1049/ipr2.12419.
[31] S. Tongbram, B. A. Shimray, and L. S. Singh, "Segmentation of image based on k-means and modified subtractive clustering," *Indonesian Journal of Electrical Engineering and Computer Science*, vol. 22, no. 3, Jun. 2021, doi: 10.11591/ijeecs.v22.i3.pp1396-1403.
[32] S. Huang, Y. Lu, W. Wang, and K. Sun, "Multi-scale guided feature extraction and classification algorithm for hyperspectral images," *Scientific Reports*, vol. 11, no. 1, Sep. 2021, doi: 10.1038/s41598-021-97636-2.

BIOGRAPHIES OF AUTHORS

Ondra Eka Putra a lecturer at the Faculty of Computer Science in Universitas Putra Indonesia YPTK Padang, West Sumatra. He was Born in Bayang, 06 June 1987. He has completed his Bachelor's degree program in Computer Systems, Universitas Putra Indonesia YPTK Padang in 2011. He has completed a Computer Master's program in Information Technology in 2013. Research work focuses specifically on image processing, artificial intellegence, and programming. He can be contacted at email: ondraekaputra@upiyptk.ac.id.

Sumijan was born in Nganjuk, East Java, Indonesia in 1966. Obtained a bachelor's degree at Putra Indonesia University YPTK. Then earned an M.Sc. from University Teknologi Malaysia and a Doctor of Information Technology from Gunadarma University in 2015. He is a lecturer at the Faculty of Computer Science in the Information Technology Program. His work focuses on image processing. He can be contacted at email: sumijan@upiyptk.ac.id.

Muhammad Tajuddin is a dedicated lecturer and Professor in the Information Technology (S3) Study Program within the Faculty of Computer Science at Universitas Putra Indonesia YPTK Padang, Sumatera Barat, Indonesia. He earned his Bachelor's Degree from Universitas Mataram in the Information System program under the Faculty of Computer Science. He pursued a Master's Degree at Universitas Brawijaya, specializing in Computer Science. He pursued a doctoral degree from Universitas Brawijaya. His academic pursuits reflect a commitment to continuous learning and scholarly excellence. His research endeavors traverse diverse domains, with particular expertise in information system. He welcomes communication and collaboration. He can be contacted at email: tajuddin@universitasbumigora.ac.id.